

# “HOT” NON-FLARING PLASMA IN ACTIVE REGIONS II. IMPACTS OF TWO-FLUID EFFECTS

W. T. BARNES AND S. J. BRADSHAW

Department of Physics & Astronomy, Rice University, Houston, TX 77251-1892

P. J. CARGILL

Space and Atmospheric Physics, The Blackett Laboratory, Imperial College, London SW7 2BW and  
 School of Mathematics and Statistics, University of St. Andrews, St. Andrews, Scotland KY16 9SS

*Draft version October 2, 2015*

## ABSTRACT

Faint, high-temperature emission in active region cores has long been predicted as a signature of nanoflare heating. However, the detection of such emission has proved difficult due to a combination of the efficiency of thermal conduction, non-equilibrium ionization, and inadequate instrument sensitivity. This second paper in our series on hot non-flaring plasma in active regions aims to show how the assumption of electron-ion equilibrium in hydrodynamic models leads to incorrect conclusions regarding the hot emission. We have used an efficient two-fluid hydrodynamic model to carry out a parameter exploration in preferentially heated species, nanoflare heating frequency, and event amplitude power-law index. By computing the emission measure distributions and calculating their “hotward” slopes, we have concluded that the assumption of electron-ion equilibrium leads to an underestimate of the amount of hot plasma at intermediate and high heating frequencies. Additionally, we find that, while emission due to electron and ion heating differs greatly hotward of the peak, the respective coolward emission measure slopes are similar such that a distinction between the heating of one species over another based on this criteria alone is inadequate.

## 1. INTRODUCTION

TODO:Include/weave in paragraph about emission measure scaling; have completely neglected thus far; maybe split between intro and methods

The nanoflare heating model, first proposed by Parker (1988), has become one of the most favored and contentious coronal heating models (Cargill 1994; Cargill & Klimchuk 2004; Klimchuk 2006). While many theoretical efforts (e.g. Bradshaw et al. 2012; Reep et al. 2013) have shown the feasibility of nanoflares, the idea has long suffered from a lack observational evidence. The term *nanoflare* has now become synonymous with impulsive heating in the energy range  $10^{24} - 10^{27}$  ergs, with no specific assumption as to what underlying physical mechanism is responsible. However, while we ascribe no particular source (e.g. wave versus reconnection) to this bursty energy release, its origin is almost certainly magnetic.

Cargill (1994); Cargill & Klimchuk (2004) have predicted that emission measure distributions resulting from nanoflare models should be wide and have a faint, high-temperature ( $> 4 \times 10^6$  K) component and thus a steep hotward slope. Unfortunately, observing this high-temperature emission is difficult and in some cases impossible. The reason for this difficulty is twofold. First, thermal conduction is a very efficient cooling mechanism at high temperatures and large spatial temperature gradients. When a loop is heated impulsively, its temperature rises quickly while the increase in density lags behind. By the time the density has increased sufficiently to allow for an appreciable amount of emission (recalling  $EM \propto n^2$ ), thermal conduction has cooled the loop far

below its initial hot temperature, making a direct detection of  $> 10$  MK plasma very difficult.

The second reason for this difficulty is non-equilibrium ionization. It is usually assumed that the observed line intensities, because of their known formation temperatures, are a direct indicator of the plasma temperature. However, if the heating timescale is shorter than the ionization timescale, the time it takes for the ion population to settle into the correct charge state, an equilibrium assumption can lead to a misdiagnosis of the plasma temperature. This makes signatures of hot, nanoflare-heated plasma especially difficult to detect if the high temperatures persist for less than the ionization timescale (Bradshaw & Cargill 2006; Bradshaw & Klimchuk 2011; Reale & Orlando 2008).

Despite these difficulties, various attempts have been made to observe this faint high-temperature emission. Using the broadband X-Ray Telescope (XRT) aboard the *Hinode* spacecraft, Schmelz et al. (2009) and Reale et al. (2009) show a faint hot component in the reconstructed DEM curves. However, since the channels on such broadband instruments can often be polluted by low-temperature emission, the reliability of such measurements depends on the filtering technique used. Additionally, Winebarger et al. (2012) showed that combinations of measurements from EIS (Culhane et al. 2007) and XRT (Golub et al. 2007) on board *Hinode* (Kosugi et al. 2007) leave a “blind spot” in the  $EM - T$  space coincident with where evidence for nanoflare heating is likely to be found.

Unambiguous observational evidence of nanoflare heating must come from pure spectroscopic measurements (see Brosius et al. 2014). Additionally, new instruments with higher spatial and temporal resolution, such as *IRIS* (De Pontieu et al. 2014) and the *Hi-C* sounding rocket

(Cirtain et al. 2013) have provided encouraging results for impulsive heating (Testa et al. 2013, 2014). Future missions like the Marshall Grazing Incidence X-ray Spectrometer (MaGIXS) (Kobayashi et al. 2011; Winebarger 2014), with a wavelength range of 6-24 Å and a temperature range of  $6.2 < \log T < 7.2$ , aim to probe this previously poorly-resolved portion of the coronal spectrum in hopes of better quantifying the presence of faint, high-temperature plasma.

Impulsive heating can also introduce electron-ion non-equilibrium. In a fully-ionized hydrogen plasma like the solar corona, interactions between electrons and ions occur through binary Coulomb collisions. For  $n \sim 10^8 \text{ cm}^{-3}$  and  $T \sim 10^7 \text{ K}$ , parameters typical of nanoflare heating, the collisional timescale,  $\tau_{ei} = 1/\nu_{ei}$ , where  $\nu_{ei}$  is the Coulomb collision frequency (see Equation A6) can be estimated as  $\tau_{ei} \sim 8000 \text{ s}$ . Thus, any heating that occurs on a timescale less than 8000 s, such as a nanoflare with a duration of  $\leq 100 \text{ s}$ , will result in electron-ion non-equilibrium.

The degree to which the ions or electrons are preferentially heated in the solar corona is unknown though it is often assumed that the electrons are the direct recipients of the prescribed heating function. However, it is also possible that the ions are preferentially heated; for instance, through ion-cyclotron wave resonances (Markovskii & Hollweg 2004). Ion cyclotron waves are excited by plasma instabilities in the lower corona. These waves then propagate upwards through the coronal plasma and wave particle interactions can occur for those ions whose gyrofrequencies have a resonance with the ion-cyclotron wave. Additionally, there is also evidence for ion heating via reconnection, both in laboratory plasmas and in particle-in-cell simulations (Ono et al. 1996; Yoo et al. 2014; Drake & Swisdak 2014). Thus, ion heating in the solar corona should not be discounted as a possibility.

In our first paper, Cargill et al. (2016) (Paper I, hereafter), we studied the effect of pulse duration, flux limiting, and non-equilibrium ionization on hot emission from single nanoflares as well as nanoflare trains. In this second paper in our series on hot emission in active region cores, we will use an efficient two-fluid hydrodynamic model to explore the effect of electron and ion heating on nanoflare-heated loops. In particular, we will look at how the hot emission is affected by heating preferentially one species or the other as well as how this hot emission can vary with heating frequency and event amplitude power-law index.

Section 2 discusses the numerical model we have used to conduct this study and the parameter space we have explored. Section 3 shows the resulting emission measure curves and slopes for the electron and ion heating cases as well as the equivalent single-fluid cases. In Section 4, we compare two-fluid and single-fluid cases for all heating functions and heating frequencies. Finally, Section 5 discusses the implications of two-fluid effects in the context of modelling impulsive heating and observing faint, hot emission, the so-called “smoking gun” of nanoflare heating.

Wouldn't be a bad idea to include summary of measured “hotward” emission slope values as is done in Bradshaw et al. (2013) for cool slopes

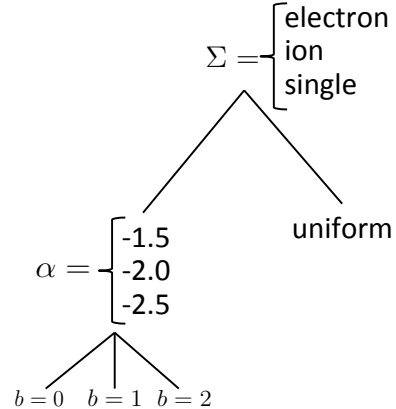


FIG. 1.— Parameter space covered for each loop half-length  $L$ .  $\Sigma$  indicates the species that is heated, where “single” indicates a single-fluid model.  $\alpha$  is the power-law index and  $b$  indicates the scaling in the relationship  $Q \propto T_N^b$ , where  $b = 0$  corresponds to the case where  $T_N$  and the event energy are independent.

## 2. METHODOLOGY

### 2.1. Numerical Model

1D hydrodynamic models are excellent tools for computing field-aligned quantities in coronal loops. However, because of the small grid sizes needed to resolve the transition region and consequently small timesteps needed to resolve thermal conduction, the use of such models in large parameter sweeps is made impractical by long runtimes (Bradshaw & Cargill 2013). Thus, in our numerical study, we will use a modified form of the popular 0D enthalpy-based thermal evolution of loops (EBTEL) model (Klimchuk et al. 2008; Cargill et al. 2012a,b, 2015) which computes time-dependent spatially-averaged loop quantities and has been successfully benchmarked against the 1D hydrodynamic HYDRAD code (Bradshaw & Cargill 2013).

We have modified the usual EBTEL equations (see Cargill et al. 2012a) to treat the evolution of the electron and ion populations separately while maintaining the assumption of quasi-neutrality,  $n_e = n_i = n$ . This amounts to computing spatial averages of the two-fluid hydrodynamic equations over both the transition region and corona. We will reserve a full discussion of this modified EBTEL model for a future paper. The relevant equations can be found in Appendix A.

### 2.2. Parameter Space

We define our heating function in terms of a series of discrete heating events plus a static background heating rate to ensure that the loop does not drop to unphysically low temperatures and densities between events. All events are modeled as triangular pulses of fixed duration  $\tau_H = 100 \text{ s}$ . Thus, for loop length  $L$  and cross-sectional area  $A$ , the total energy per event is  $Q_i = LAH_i\tau_H/2$ , where  $H_i$  is the heating rate amplitude for the  $i$ th event. Each run will consist of  $N$  heating events, with peak amplitude  $H_i$  and a steady background value of  $H_b = 3.4 \times 10^{-6} \text{ erg cm}^{-3} \text{ s}^{-1}$ .

Observations have suggested that loops in active region cores are maintained at an equilibrium temperature of  $T_{peak} \approx 4 \text{ MK}$  (Warren et al. 2011, 2012). The corresponding heating rate can be estimated using coronal

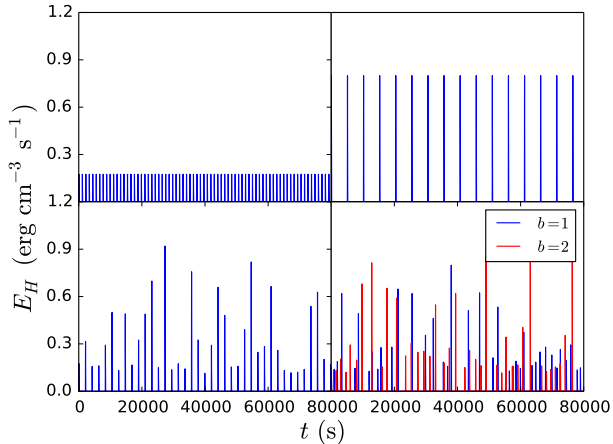


FIG. 2.— All heating functions are for  $L = 40$  Mm. Starting counter-clockwise from the bottom left: uniform heating amplitudes for  $T_N = 1000$  s; uniform heating amplitudes for  $T_N = 5000$  s; power-law distributed heating amplitudes for  $\alpha = -1.5$ ,  $T_N = 2000$  s; power-law distributed amplitudes for  $\alpha = -1.5$  where the wait times depend on the event energies and the mean wait time for both  $b$  values is  $\langle T_N \rangle = 2000$  s.

hydrostatics. Neglecting the radiative loss term and letting  $dF_C/ds \approx \kappa_0 T_{peak}^{7/2}/L^2$ ,  $E_{H,eq}$  can be estimated as

$$E_{H,eq} \approx \frac{\kappa_0 T_{peak}^{7/2}}{L^2}, \quad (1)$$

where  $\kappa_0 \approx 10^{-6}$ .  $E_{H,eq}$  can be interpreted as a time-averaged volumetric heating rate. Thus, to maintain an emission measure peaked about  $T_{peak}$ , for triangular pulses, the individual heating rates are constrained by

$$E_{H,eq} = \frac{1}{T} \sum_{i=1}^N \int_{t_i}^{t_i + \tau_H} dt h_i(t) = \frac{\tau_H}{2T} \sum_{i=1}^N H_i. \quad (2)$$

Note that if  $H_i = H_0$  for all  $i$ , the uniform heating amplitude  $H_0$  is just  $H_0 = 2TE_{H,eq}/N\tau_H$ . Thus, for  $L = 40$  Mm,  $A = 10^{14}$  cm<sup>2</sup>, the total amount of energy injected into the loop by one heating event for a loop heated by  $N = 20$  nanoflares in  $T = 80000$  s is  $Q = LA TE_{H,eq}/N \approx 1.3 \times 10^{25}$  erg, consistent with the energy budget of the Parker nanoflare model.

Determining the heating frequency in active region cores will help to place constraints on the source(s) of heat in the corona. We define the heating frequency in terms of the waiting time,  $T_N$ , between successive heating events. Following Cargill (2014), the range of waiting times is  $250 \leq T_N \leq 5000$  s in increments of 250 s, for a total of 20 different possible heating frequencies. Additionally,  $T_N$  can be written as  $T_N = (T - N\tau_H)/N$ , where  $T = 80000$  s is the total simulation time. Note that because  $T$  and  $\tau_H$  are fixed, as  $T_N$  increases,  $N$  decreases. Correspondingly,  $Q_i$ , the energy injected per event, increases according to Equation 2 such that the total energy injected per run is constant, regardless of  $T_N$ .

We compute the peak heating rate per event in two different cases: 1) uniform heating rate such that  $H_i = H_0$  for all  $i$  and 2)  $H_i$  chosen from a power-law distribution with index  $\alpha$  where  $\alpha = -1.5, -2.0, -2.5$ . For the

second case, it should be noted that, when  $T_N$  is large,  $N \sim 20$  events, meaning a single run does not accurately represent the distribution of index  $\alpha$ . Thus, a sufficiently large number of runs,  $N_{MC}$ , are computed for each  $T_N$  to ensure that the total number of events is  $N_{tot} = N \times N_{MC} \sim 10^4$  such that the distribution is well-represented. Figure 1 shows the parameter space we will explore. For each point in  $(\Sigma, \alpha, b)$  space, the response to  $\sim N_{tot}$  events for each waiting time  $T_N$  will be computed.

According to the nanoflare heating model of (Parker 1988), turbulent loop footpoint motions twist and stress the field, leading to a buildup and subsequent release of energy. Following Cargill (2014), we let  $Q_i \propto T_{N,i}^b$ , where  $Q_i, T_{N,i}$  are the total energy and waiting time following the  $i$ th event, respectively, and  $b = 1, 2$ . The reasoning for such an expression is as follows. Bursty, nanoflare heating is thought to arise from the stressing and subsequent relaxation of the coronal field. If a sufficient amount of time has elapsed since the last energy release event, the field will have had enough time to “wind up” such that the subsequent energy release is large. Conversely, if only a small amount of time has elapsed since the last event, the field will have not had time to become as stressed, resulting in a lower energy event. Thus, this scaling provides a way to incorporate a more realistic heating function into a hydrodynamic model which cannot self-consistently determine the heat input based on the evolving magnetic field. Figure 2 shows the various heating functions used for several example  $T_N$  values.

### 2.3. Emission Measure Distributions

In our 0D model, the emission measure is calculated using the familiar expression  $EM(T) = n^2(2L)$ , where  $L$  is the loop half-length. We consider a temperature range of  $4.0 \leq \log T \leq 8.5$  with bin sizes of  $\Delta \log T = 0.01$ . At each iteration  $i$ , the coronal temperature range  $[T_0, T_a]$  is calculated from  $\bar{T}_e$  (see Appendix A). For each bin that falls within  $[T_0, T_a]$ ,  $\bar{n}_i^2 L$  is added to that bin, where  $\bar{n}_i$  is the spatially-averaged number density at the  $i$ th iteration. After all iterations have completed, the emission measure in each bin is averaged over the entire simulation period. We do not attempt to apply an advanced forward modeling treatment here and instead reserve such an approach for a future paper. Thus, effects due to insufficient instrument sensitivity or non-equilibrium ionization are not included.

## 3. RESULTS

### 3.1. Electron and Ion Heating

For each species, power-law and wait-time index,  $(\alpha, b)$ , and waiting time  $T_N$ ,  $N_{MC}$  emission measure curves are calculated. Because drawing event amplitudes from a power-law distribution introduces random fluctuations into our model, we must be sure to account for the full range of effects due to the distribution. This is especially true in the low-frequency regime, when  $T_N \geq \tau_{cool}$ , and there are fewer events per run. In this case, one or two especially strong heating events can lead to an extremely enhanced hotward emission measure; conversely, a run with only small events will lead to a diminished hotward slope. Thus, the mean  $EM(T)$  curve of each set of  $N_{MC}$  runs can be said to reasonably represent the expected

hot emission for a given  $T_N$ .

To characterize the emission measure, we compute the slopes on both the cool and hot sides of the peak. To be consistent with past observational and computational studies of cool emission (see Bradshaw et al. 2012, and references therein), we fit the cool slope on the interval  $[6.0, 6.6]$  in  $\log T$ . Contrastingly, past studies of hot emission are less abundant; thus, the region where  $\log EM(T)$  is known to be linear is far less constrained. In order to best describe the steepness of the emission measure hotward of the peak, we choose to fit  $EM(T)$  between the temperature at which the emission measure is 99% of the peak value and 92% of the peak value. We have no physical reason for choosing these particular bounds, but note that on this interval, the mean hotward emission is reasonably well described by a linear relationship. Fitting too close to the wide peak leads to misleadingly shallow slopes while fitting too close to the steep drop near  $\log T \sim 7.5$  results in steep slopes not particularly representative of the hotward emission. We perform the fit using the Levenberg-Marquardt algorithm for least-squares curve fitting as implemented in the SciPy scientific Python package (van der Walt et al. 2011).

Figure 3 and Figure 4 show the results of our emission measure study for the cases of electron heating and ion heating with  $\alpha = -2.5, b = 1$  for a loop half-length of 40 Mm, consistent with Paper I. The panels on the left show the mean  $EM(T)$  for all  $T_N$ , where the average is taken over all  $N_{MC}$  runs. There is an artificial spacing

of  $\Delta \log EM = 0.2$  between each curve so that they can be easily distinguished from each other. The blue (red) lines indicate the cool (hot) linear fits, where the slopes of the lines are the averages taken over all  $N_{MC}$  runs. The top right panels show these average slope values as a function of  $T_N$ . The error bars indicate one standard deviation as calculated from the distribution of all  $N_{MC}$  runs. In the case of the hot slopes, the absolute value of the slope is shown since all of the hotward slopes are less than zero.

Lastly, the bottom right panels show the first derivative as a function of temperature,  $d \log EM / d \log T$ , computed using central differences. The color scheme and line styles correspond to the emission measure curves in the left panel. As in Paper I, we compute the derivative in an effort to better assess at what temperatures the emission measure is not well described by a linear fit.

### 3.2. Single-fluid

EM plot, derivs plot, slope plot

## 4. DISCUSSION

place histograms here maybe...

## 5. CONCLUSION

## ACKNOWLEDGMENT

## APPENDIX

The modified two-fluid EBTEL equations are,

$$\frac{d}{dt} \bar{p}_e = \frac{\gamma - 1}{L} [\psi_{TR} + \psi_C - (\mathcal{R}_{TR} + \mathcal{R}_C)] + k_B \bar{n} \nu_{ei} (\bar{T}_i - \bar{T}_e) + (\gamma - 1) \bar{E}_{H,e}, \quad (\text{A1})$$

$$\frac{d}{dt} \bar{p}_i = -\frac{\gamma - 1}{L} (\psi_{TR} + \psi_C) + k_B \bar{n} \nu_{ei} (\bar{T}_e - \bar{T}_i) + (\gamma - 1) \bar{E}_{H,i}, \quad (\text{A2})$$

$$\frac{d}{dt} \bar{n} = \frac{c_2(\gamma - 1)}{c_3 \gamma L k_B \bar{T}_e} (\psi_{TR} - F_{e,0} - \mathcal{R}_{TR}), \quad (\text{A3})$$

where

$$\psi_{TR} = \frac{1}{1 + \xi} (F_{0,e} + \mathcal{R}_{TR} - \xi F_{0,i}), \quad (\text{A4})$$

$$\psi_C = \bar{v} p_e^{(a)} - (p_e v)_0. \quad (\text{A5})$$

Additionally, Equation A1, Equation A2, and Equation A3 are closed by the equations of state  $p_e = k_B n T_e$  and  $p_i = k_B n T_i$ .

The volumetric heating rates,  $E_{H,e}$  and  $E_{H,i}$ , are the primary degrees of freedom in our model. In the case of electron (ion) heating,  $E_{H,i}$  ( $E_{H,e}$ ) = 0.  $\bar{p}_e, \bar{p}_i$  and  $\bar{T}_e, \bar{T}_i$  are the spatially-averaged coronal electron and ion pressures and temperatures, respectively and  $\bar{n}$  is the spatially-averaged coronal number density.  $\mathcal{R}_C = \bar{n}^2 \Lambda(T)$  is the volumetric coronal radiative loss rate, where  $\Lambda(T)$  is the radiative loss function, and  $\mathcal{R}_{TR} = c_1 \mathcal{R}_C$  is the radiative loss rate in the transition region where the calculation of  $c_1$  is described in Cargill et al. (2012a). Additionally,  $F_{e,0}, F_{i,0}$  are the electron and ion conductive fluxes as computed at the base of the loop, respectively, and are calculated using the classical Spitzer formula with a flux limiter imposed to prevent runaway cooling at low densities. The Coulomb collision frequency,  $\nu_{ei}$ , is given by,

$$\nu_{ei} = \frac{16\sqrt{\pi}}{3} \frac{e^4}{m_e m_i} \left( \frac{2k_B \bar{T}_e}{m_e} \right)^{-3/2} \bar{n} \ln \Lambda, \quad (\text{A6})$$

where  $m_e, m_i$  are the electron and ion masses respectively and  $\ln \Lambda$  is the Coulomb logarithm. Finally,  $c_2 = \bar{T}/T_a = 0.6$ ,  $c_3 = T_0/T_a = 0.9$ , determined by static equilibrium, and  $\xi = \bar{T}_e/\bar{T}_i$ .



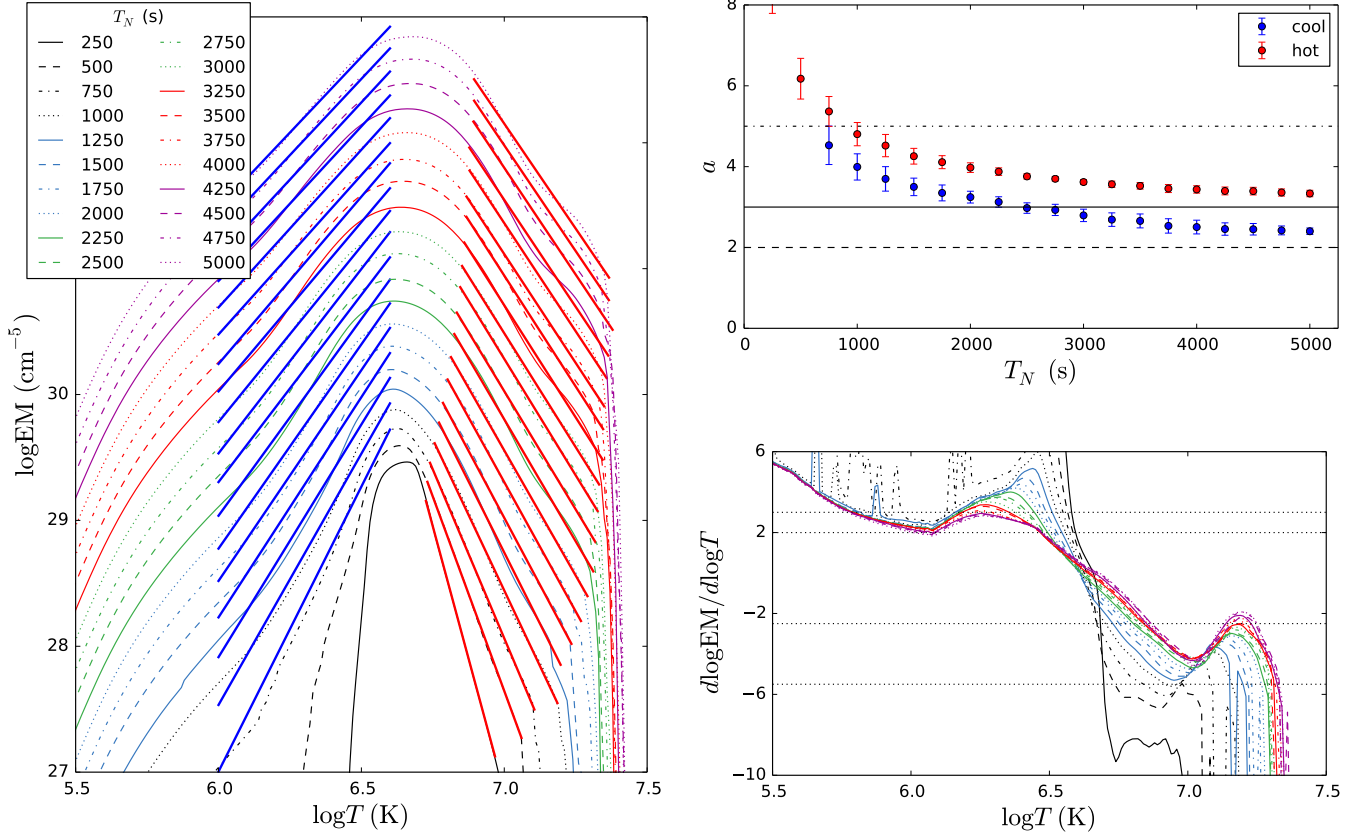


FIG. 3.— **TODO: need caption describing figure.**

Note that in the limit that  $\bar{T}_e = \bar{T}_i$  such that  $\xi = 1$ , Equation A3 reduces to the single-fluid density equation of Cargill et al. (2012a). Additionally, Equation A1 and Equation A2 can be added together to recover the single-fluid pressure equation. As with the original EBTEL model, the modified two-fluid version has been successfully benchmarked against the HYDRAD hydrodynamic code.

#### REFERENCES

- Bradshaw, S. J., & Cargill, P. J. 2006, *Astronomy and Astrophysics*, 458, 987  
—, 2013, *The Astrophysical Journal*, 770, 12  
Bradshaw, S. J., & Klimchuk, J. A. 2011, *The Astrophysical Journal Supplement Series*, 194, 26  
Bradshaw, S. J., Klimchuk, J. A., & Reep, J. W. 2012, *The Astrophysical Journal*, 758, 53  
Brosius, J. W., Daw, A. N., & Rabin, D. M. 2014, *The Astrophysical Journal*, 790, 112  
Cargill, P. J. 1994, *The Astrophysical Journal*, 422, 381  
—, 2014, *The Astrophysical Journal*, 784, 49  
Cargill, P. J., Bradshaw, S. J., & Barnes, W. T. 2016, in preparation  
Cargill, P. J., Bradshaw, S. J., & Klimchuk, J. A. 2012a, *The Astrophysical Journal*, 752, 161  
—, 2012b, *The Astrophysical Journal*, 758, 5  
Cargill, P. J., & Klimchuk, J. A. 2004, *The Astrophysical Journal*, 605, 911  
Cargill, P. J., Warren, H. P., & Bradshaw, S. J. 2015, *Phil. Trans. R. Soc. A*, 373, 20140260  
Cirtain, J. W., Golub, L., Winebarger, A. R., et al. 2013, *Nature*, 493, 501  
Culhane, J. L., Harra, L. K., James, A. M., et al. 2007, *Solar Physics*, 243, 19  
De Pontieu, B., Title, A. M., Lemen, J. R., et al. 2014, *Solar Physics*, 289, 2733  
Drake, J. F., & Swisdak, M. 2014, *Physics of Plasmas* (1994-present), 21, 072903  
Golub, L., Deluca, E., Austin, G., et al. 2007, *Solar Physics*, 243, 63  
Klimchuk, J. A. 2006, *Solar Physics*, 234, 41  
Klimchuk, J. A., Patsourakos, S., & Cargill, P. J. 2008, *The Astrophysical Journal*, 682, 1351  
Kobayashi, K., Cirtain, J., Golub, L., et al. 2011, in *Society of Photo-Optical Instrumentation Engineers (SPIE) Conference Series*, Vol. 8147, 81471M  
Kosugi, T., Matsuzaki, K., Sakao, T., et al. 2007, *Solar Physics*, 243, 3  
Markovskii, S. A., & Hollweg, J. V. 2004, *The Astrophysical Journal*, 609, 1112  
Ono, Y., Yamada, M., Akao, T., Tajima, T., & Matsumoto, R. 1996, *Physical Review Letters*, 76, 3328  
Parker, E. N. 1988, *The Astrophysical Journal*, 330, 474  
Reale, F., & Orlando, S. 2008, *The Astrophysical Journal*, 684, 715  
Reale, F., Testa, P., Klimchuk, J. A., & Parenti, S. 2009, *The Astrophysical Journal*, 698, 756  
Reep, J. W., Bradshaw, S. J., & Klimchuk, J. A. 2013, *The Astrophysical Journal*, 764, 193  
Schmelz, J. T., Saar, S. H., DeLuca, E. E., et al. 2009, *The Astrophysical Journal Letters*, 693, L131  
Testa, P., De Pontieu, B., Martinez-Sykora, J., et al. 2013, *The Astrophysical Journal Letters*, 770, L1  
Testa, P., De Pontieu, B., Allred, J., et al. 2014, *Science*, 346, 1255724  
van der Walt, S., Colbert, S. C., & Varoquaux, G. 2011, *Computing in Science & Engineering*, 13, 22  
Warren, H. P., Brooks, D. H., & Winebarger, A. R. 2011, *The Astrophysical Journal*, 734, 90  
Warren, H. P., Winebarger, A. R., & Brooks, D. H. 2012, *The Astrophysical Journal*, 759, 141  
Winebarger, A. R. 2014, *AGU Fall Meeting Abstracts*, 52, 03

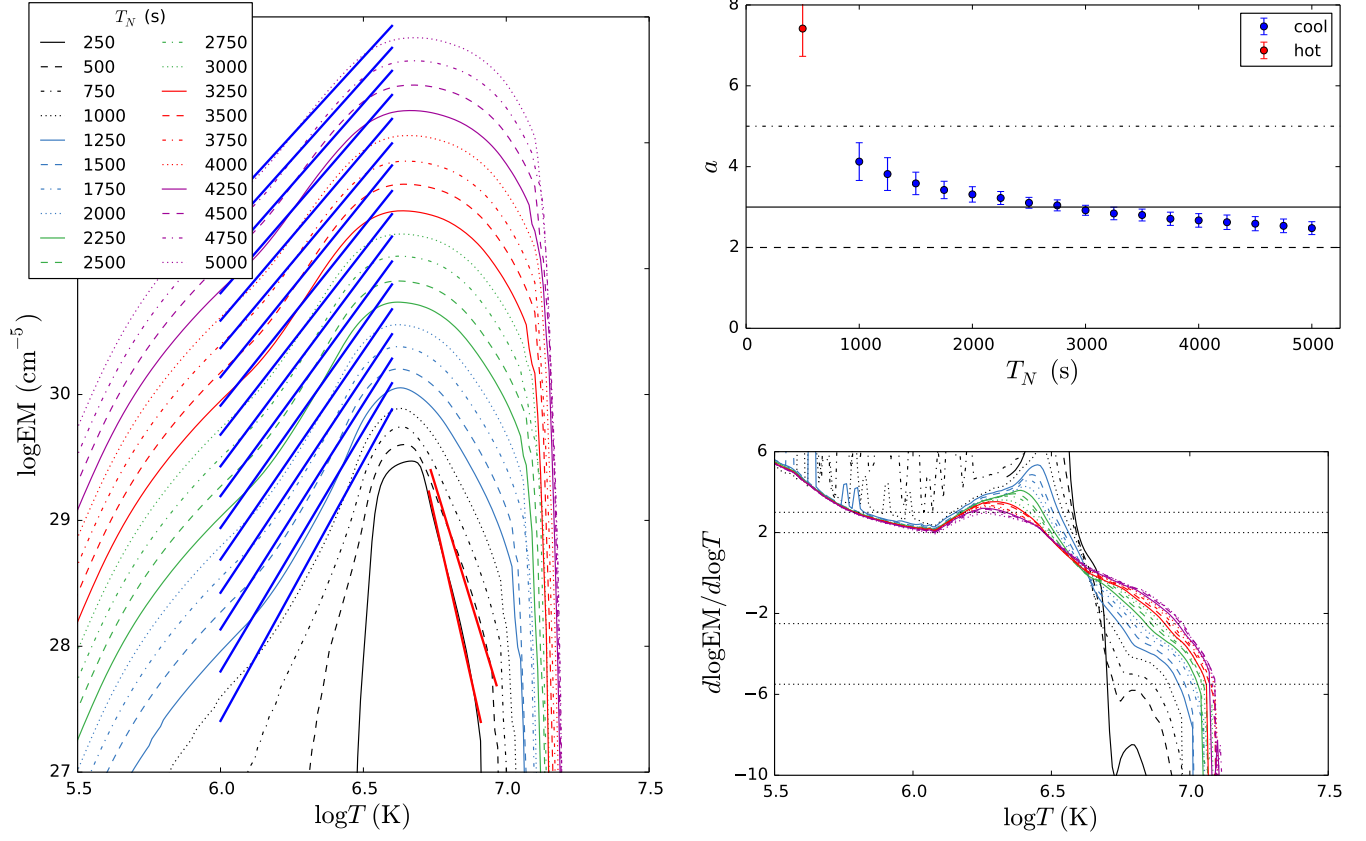


FIG. 4.— Same as Figure 3, but for the case in which all of the heating is given to the ions.

Winebarger, A. R., Warren, H. P., Schmelz, J. T., et al. 2012,  
The Astrophysical Journal Letters, 746, L17

Yoo, J., Yamada, M., Ji, H., Jara-Almonte, J., & Myers, C. E.  
2014, Physics of Plasmas (1994-present), 21, 055706

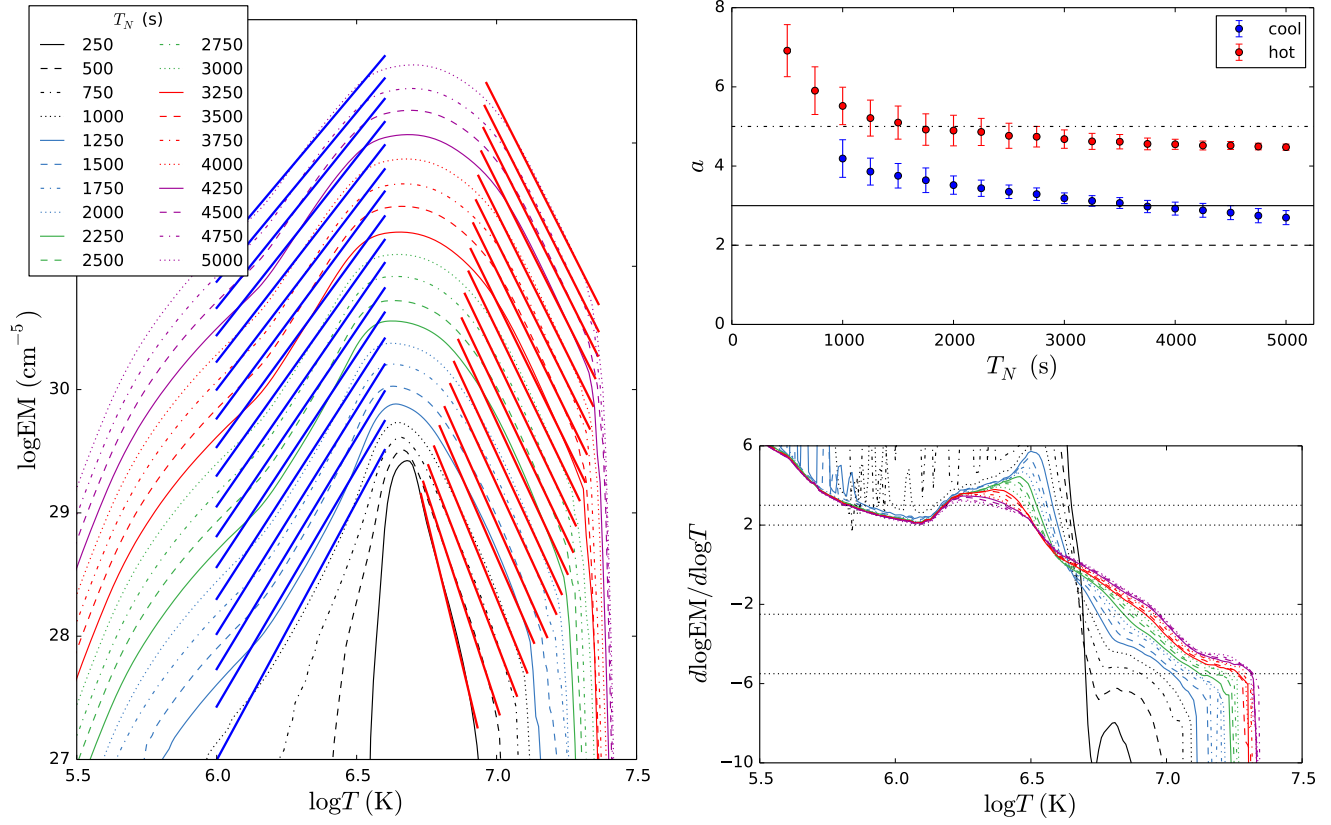


FIG. 5.— Same as Figure 3, but for the single-fluid case in which electron-ion equilibrium is assumed.